

# Optical and X-Ray Observations of GRB 060526: A Complex Afterglow with An Achromatic Jet Break

X. Dai<sup>1</sup>, J. P. Halpern<sup>2</sup>, N. D. Morgan<sup>1</sup>, E. Armstrong<sup>3</sup>, N. Mirabal<sup>2,4</sup>, J. B. Haislip<sup>5</sup>,  
D. E. Reichart<sup>5</sup>, and K. Z. Stanek<sup>1</sup>

xinyu@astronomy.ohio-state.edu

## ABSTRACT

We obtained 98  $R$ -band and 18  $B$ ,  $r'$ ,  $i'$  images of the optical afterglow of GRB 060526 ( $z = 3.21$ ) with the MDM 1.3m, 2.4m, and the PROMPT telescopes in Cerro Tololo over the 5 nights following the burst trigger. Combining these data with other optical observations reported in GCN and the *Swift*-XRT observations, we compare the optical and X-ray afterglow light curves of GRB 060526. Both the optical and X-ray afterglow light curves show rich features, such as flares and breaks. The densely sampled optical observations provide very good coverage at  $T > 10^4$  sec. We observed a break at  $2.4 \times 10^5$  sec in the optical afterglow light curve. Compared with the X-ray afterglow light curve, the break is consistent with an achromatic break supporting the beaming models of GRBs. However, the pre-break and post-break temporal decay slopes are difficult to explain in simple afterglow models. We estimated a jet angle of  $\theta_j \sim 7^\circ$  and a prompt emission size of  $R_{prompt} \sim 2 \times 10^{14}$  cm. In addition, we detected several optical flares with amplitudes of  $\Delta m \sim 0.2, 0.6,$  and  $0.2$  mag. The X-ray afterglows detected by *Swift* have shown complicated decay patterns. Recently, many well-sampled optical afterglows also show decays with flares and multiple breaks. GRB 060526 provides an additional case of such a complex, well observed optical afterglow. The accumulated well-sampled afterglows indicate that most of the optical afterglows are complex.

*Subject headings:* gamma rays: bursts

---

<sup>1</sup>Department of Astronomy, Ohio State University, Columbus, OH 43210.

<sup>2</sup>Department of Astronomy, Columbia University, 550 West 120th Street, New York, NY 10027.

<sup>3</sup>Department of Physics, University of California, San Diego, CA 92093.

<sup>4</sup>Department of Astronomy, University of Michigan, Ann Arbor, MI 48109.

<sup>5</sup>Department of Physics and Astronomy, University of North Carolina, Chapel Hill, NC 27599.

## 1. Introduction

In the fireball model (Mészáros & Rees 1997; Sari et al. 1998), the afterglow emission of gamma-ray bursts (GRBs) are thought to be synchrotron emission in the external shocks. After the launch of *Swift* (Gehrels et al. 2004), with its rapid localization of GRBs and the dedicated on-board XRT instrument, the afterglow models can be tested extensively with the regularly obtained XRT light curves. More than half of the *Swift*-XRT light curves show complicated decay patterns with multiple breaks and giant X-ray flares (Nousek et al. 2006; O’Brien et al. 2006). New ingredients were added to the models to interpret these features (e.g., Zhang et al. 2006). Compared with the large number of *Swift*-XRT afterglows, only a few bursts have good optical afterglow coverage, which limits the multi-wavelength study of GRB afterglows. Moreover, a large fraction of the well-studied optical afterglows also show complicated behaviors (e.g., GRB 060206 and GRB 060210, Stanek et al. 2006), challenging the simple, smooth-decay afterglow models. Given the current status of the field, it is important to expand the number of bursts with well-sampled afterglow light curves.

Another important aspect of the models is that GRBs are thought to be collimated in jets, based on the achromatic breaks observed in many optical GRB afterglow light curves (e.g., Stanek et al. 1999). Different jet models have been proposed for GRBs either under a uniform jet model (Rhoads 1999; Frail et al. 2001) or a structured jet model (Zhang & Mészáros 2002a; Rossi et al. 2002; Lloyd-Ronning et al. 2004; Zhang et al. 2004; Dai & Zhang 2005). Some of these jet models can also unify the closely related phenomena of X-ray flashes with GRBs (Yamazaki et al. 2003; Zhang et al. 2004; Lamb et al. 2005; Dai & Zhang 2005). Since the distinct signature that a jet imposes on GRB afterglow light curves (an achromatic break) is simply a geometric effect, it is important to test the wavelength independence across the broadest possible wavelength range, for example between optical and X-ray afterglow light curves. To date, the lack of wavelength dependence has only been confirmed across different optical bands. Recently, GRB 050525A (Blustin et al. 2006), GRB 050801 (Rykoff et al. 2006), and GRB 060206 (Stanek et al. 2006) show possible achromatic breaks across optical and X-ray light curves. However, in GRB 050801, the break is interpreted as energy injection or the onset of the afterglow, and in GRB 060206, it is debated whether the break is achromatic (Monfardini et al. 2006).

As many XRT light curves show multiple breaks, it is not obvious which of them should be associated with the optical break and which of them interpreted as the jet break. Recently, Panaitescu et al. (2006) showed that some of the X-ray breaks (1–4 hours after the burst trigger) are chromatic from X-rays to optical bands. These observations have cast doubt on the beaming models of GRBs. However, as the X-ray light curves have several breaks, it is possible that the achromatic jet break occurs at some later time. In addition, as many

optical afterglows also show rich features such as flares and multiple breaks (e.g., Stanek et al. 2006), fits to poorly sampled optical light curves may not be reliable.

In this paper, we report the optical follow-up of GRB 060526 with the MDM 1.3m, 2.4m telescopes and the PROMPT at Cerro Tololo, and our detection of an achromatic break across the optical and X-ray bands. GRB 060526 was detected by the BAT on board *Swift* at 16:28:30 UT on May 26, 2006 (Campana et al. 2006). The XRT and UVOT rapidly localized the burst location. The burst was followed up with ground-based telescopes by several groups. In particular, Berger & Gladders (2006) reported the burst redshift of  $z = 3.21$ . We organize the paper as follows. First, we describe the data reduction in §2. In §3, we describe the evolution of the GRB afterglow and perform a comparison between the optical and X-ray light curves. Finally, we discuss our results in §4.

## 2. The Optical and X-ray Data Reduction

We obtained 83 and 15 optical *R*-band exposures with the MDM 1.3m, 2.4m telescopes, and 18 *B*, *r'*, *i'* images with the PROMPT in Cerro Tololo, respectively, on the nights of 26–30 May 2006. After standard bias subtraction and flatfielding, we measured relative fluxes between GRB 060526 and six nearby reference stars that had been calibrated using the Landolt (1992) standard field on the 1.3m. The local reference stars also served to tie the 2.4m data onto the 1.3m photometric system, with typical rms scatter of the 2.4m zeropoint determination of 0.02–0.03 magnitudes for each epoch. In general, overlapping GRB 060526 data between the two telescopes agreed to within the computed error bars (see Fig. 2). As GRB 060526 was a bright burst observed by many groups, we also collected other *R*-band observations reported in the GCN circulars (French & Jelinek 2006; Covino et al. 2006; Lin et al. 2006; Khamitov et al. 2006a,b,c,d,e,f; Rumyantsev et al. 2006a,b; Kann & Hoegner 2006; Baliyan et al. 2006; Terra et al. 2006). When the reference stars and their magnitudes were given, we calibrated their magnitudes to our magnitude system.

We also reduced the *Swift*-XRT data for GRB 060526. The XRT observations cover 6 days with gaps in between for the burst. We analyzed the XRT level 2 event files for both the windowed timing (WT) and photon counting (PC) modes. These events were filtered to be within 0.2–10 keV energy band and restricted to grades of 0–2 for the WT mode and 0–12 for the PC mode. We extracted the XRT spectra and light-curves with the software tool `xselect`<sup>1</sup>. We use the `rmf` files from the standard XRT calibration distribution, and

---

<sup>1</sup><http://heasarc.gsfc.nasa.gov/docs/software/lheasoft/ftools/xselect/xselect.html>.

generated the `arf` files with the *Swift*-XRT software tool <sup>2</sup>. Finally, we fit the X-ray spectra with XSPEC (Arnaud 1996).

### 3. Evolution of the Afterglow

The overall optical and X-ray light-curves of GRB 060526 are shown in Fig. 1, and data are listed in Table 1. In addition, we also show the densely sampled optical data in more detail in Fig. 2. Both the optical and X-ray light curves exhibit rich features including flares and breaks beyond a simple power-law decay. Below, we discuss the evolution of the optical and X-ray light curves separately at first and then compare them afterward. Following the literature, we model the segments of the afterglow with single power-laws of  $f_\nu \propto t^{-\alpha} \nu^{-\beta}$ . We also used the broken power-law for the temporal decay in some cases as  $f(t) \propto ((\frac{t}{t_b})^{\alpha_e s} + (\frac{t}{t_b})^{\alpha_l s})^{-1/s}$ , where  $\alpha_e$ ,  $\alpha_l$ ,  $t_b$ , and  $s$  are the early and late decay indices, break time, and smoothness parameters, respectively. We fixed the smoothness parameter to  $s = 2.5$  for our analysis.

The optical light curve shows at least one break at  $T \sim 2.4 \times 10^5$  sec and possibly an earlier one at  $T \sim 10^4$  sec. In addition, we detect multiple optical flares in our densely sampled regions. As we only have few data points for the early afterglow light curve, we focus on the period after  $10^4$  sec. The light curve between  $10^4 < T < 5.4 \times 10^4$  sec is well fitted by a power-law with a slope of  $1.14 \pm 0.02$  (Fig. 2). In the period between  $5.4 \times 10^4 < T < 2.0 \times 10^5$  sec, several optical flares occurred, based on the shape of the light curve and the extrapolation of the power-law decay slope from the previous stage. The flares peak at  $\sim 6.1 \times 10^4$ ,  $1.2 \times 10^5$ , and  $1.8 \times 10^5$  sec with peak magnitude changes of  $\Delta m \sim 0.2, 0.6$ , and  $0.2$  mag, respectively, above a power-law extrapolation from the previous period, and the durations of flares,  $\Delta t$ , are  $\sim 10^4$  sec,  $7 \times 10^4$  sec, and  $4 \times 10^4$  sec. After the flares, the light curve steepens ( $T > 2.4 \times 10^5$  sec) as a power-law, and we find an index of  $3.4 \pm 0.2$ , assuming that the optical flares do not contribute to this part of the light curve. If we treat the optical afterglow light curve as the “bump and wiggle” modification of the smooth afterglow instead of flares on top of a smooth afterglow, we fit all the optical data points ( $T > 10^4$  sec) with a broken power-law and we find early and late decay slopes of  $\sim 1.0$  and  $\sim 2.9$  and a break time at  $\sim 2.2 \times 10^5$  sec. This fit is statistically unacceptable because it cannot describe the “bump and wiggle” part of the afterglow. We estimated the optical spectral index from the  $B, r', i'$  images taken by the PROMPT close to  $4 \times 10^4$  sec and obtained  $\beta_o = 1.69^{+0.53}_{-0.49}$  (Fig. 3). We have taken account of the effects from Galactic

---

<sup>2</sup>[http://swift.gsfc.nasa.gov/docs/swift/analysis/xrt\\_swguide\\_v1.2.pdf](http://swift.gsfc.nasa.gov/docs/swift/analysis/xrt_swguide_v1.2.pdf).

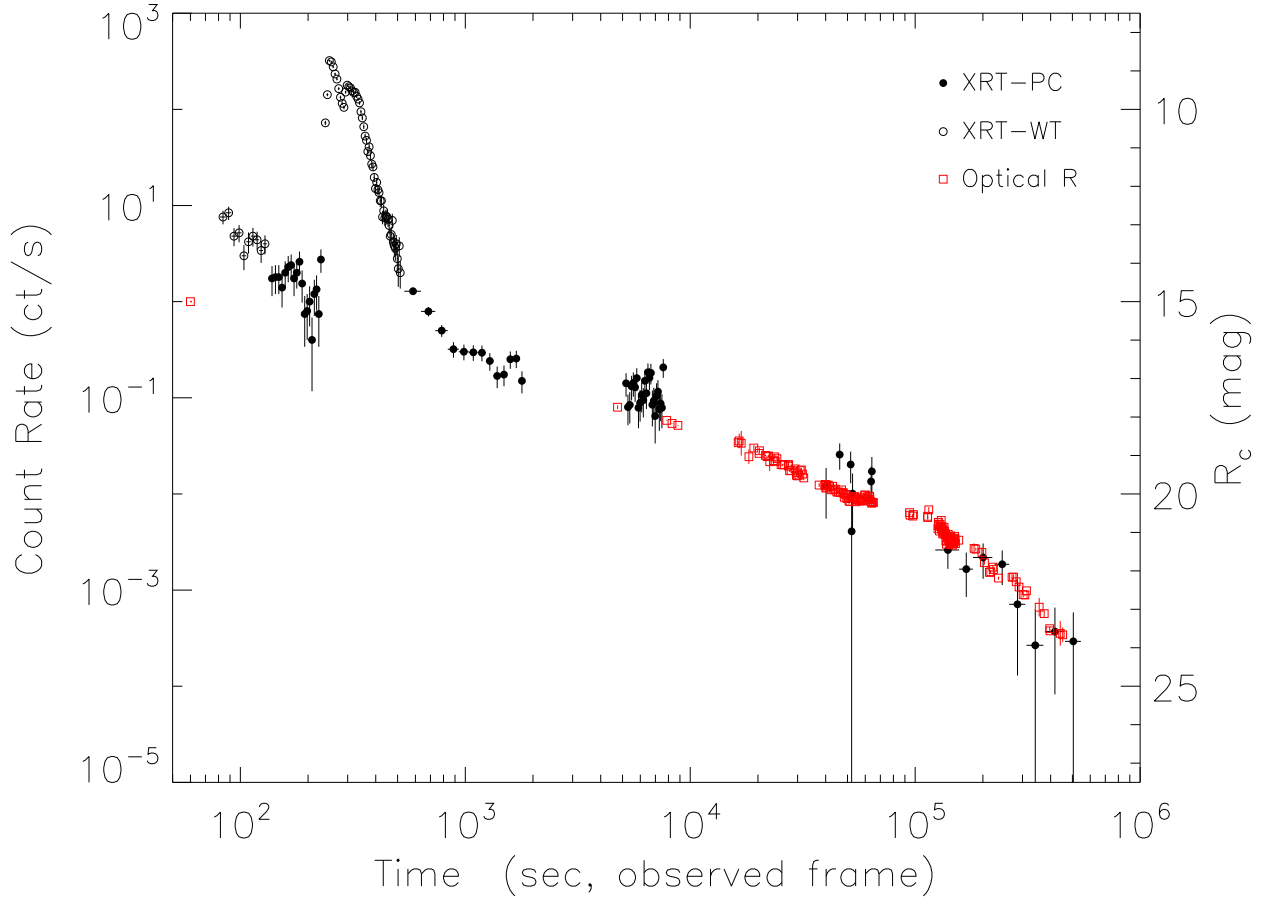


Fig. 1.— X-ray and optical afterglow light curves of GRB 060526. The open and filled circles are data from the XRT Windowed Timing mode and Photon Counting mode, respectively, and the red squares are the R band optical data from our MDM 1.3m, 2.4m, and PROMPT observations combined with other optical observations reported in the GCN. The normalization between the optical and X-ray light curves is  $f_o/f_x \sim 1000$  for the late afterglow light curve ( $T > 3 \times 10^4$  sec), and the optical to X-ray spectral index is  $\beta_{ox} \sim 1.0$ .

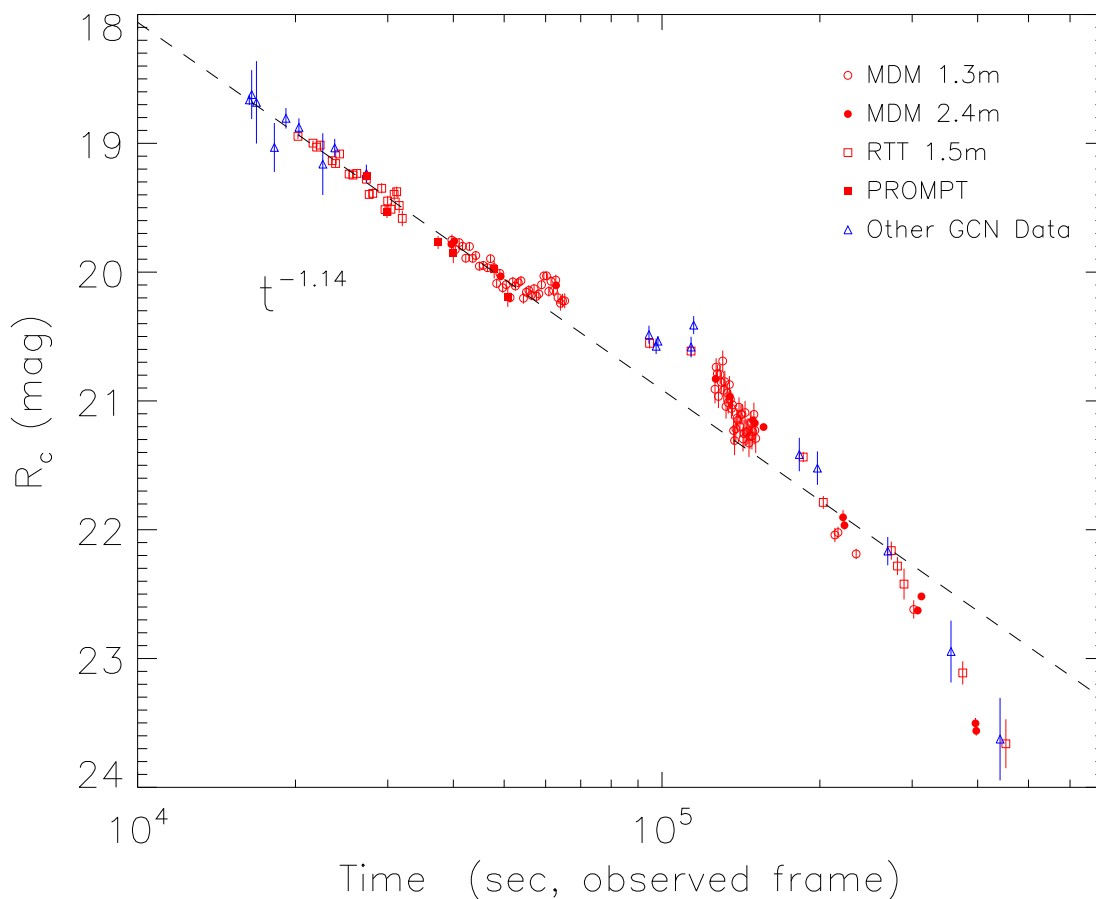


Fig. 2.— The densely sampled optical light curve from  $10^4$  sec after the burst trigger. The open circles, filled circles, and fill squares are our MDM 1.3m, 2.4m, and PROMPT observations and the rest of the data are from GCN circulars. The data before  $5.4 \times 10^4$  sec is fitted by a power-law with a slope of  $1.14 \pm 0.02$  (dashed line). Compared with the single power-law fit, the late optical data clearly show multiple flares and a much steeper late time decay slope of  $3.4 \pm 0.2$ .

extinction and the Ly $\alpha$  forest.

The X-ray light curve also cannot be fitted by a single power-law model. The most striking features are the two X-ray flares between 225 and 600 sec after the burst trigger. We find that the flares peak at  $T = 250$  sec and  $T = 300$  sec after the trigger, consistent with the GCN report (Campana et al. 2006). Even if we neglect the data points dominated by the two X-ray flares, the light curve still cannot be fitted with a single power-law. The light curve can be fitted with several power-law segments, as with many other XRT afterglow light curves observed with *Swift* (Nousek et al. 2006) and theoretical models (Zhang et al. 2006). Besides the breaks and the two giant flares, the X-ray light curve also shows small amplitude variability between  $5000 < T < 8000$  sec and possibly between  $4 \times 10^4 < T < 6.4 \times 10^4$  sec. The XRT light curve decays as  $\alpha_1 = 2.3 \pm 0.2$  at  $T < 225$  sec before the flares. After the two X-ray flares, the X-ray emission decays slowly with  $\alpha_2 \sim 0.5$  between  $850 < T < 8000$  sec. The extrapolation of the shallow decay slope does not fit the remaining data point, and the rest of the afterglow evolution is expected to follow the “normal+jet” decay stage. However, the exact time of the transition is unknown because of the gaps in the XRT light curve. If we assume the transition occurs at between  $5000 < T < 8000$  sec and fit the data points at  $T > 5000$  sec with a broken power-law model, we obtained  $\alpha_3 \sim 1.1$ ,  $\alpha_4 \sim 3.3$ , and  $T_b \sim 2.3 \times 10^5$  sec. We also fitted the X-ray light curve after the two giant flares ( $T > 850$  sec) using a single break and obtained a good fit with  $\alpha_2 \sim 0.5$ ,  $\alpha_3 \sim 1.6$ , and  $T_b \sim 2 \times 10^4$  sec. Essentially, this is equivalent to replacing the previous “normal+jet” model with a single power-law decay of slope 1.6. Finally, we analyzed the X-ray spectra of the GRB afterglow for several stages and show the evolution in Fig. 3. We detected spectral evolution before and after the two X-ray flares. After the X-ray flares, we found the X-ray spectral indices are roughly consistent except that the index for the shallow decay stage ( $\alpha_2 \sim 0.5$ ) is slightly harder.

The late optical light curve ( $T > 10^4$  sec) clearly shows a break at  $2.4 \times 10^5$  sec, while the X-ray light curve can be modeled both as a broken power-law and single power-law. If the X-ray light curve decays as a single power-law at this stage, it obviously does not follow the optical afterglow. On the other hand, the fitting results of the broken power-law model for the X-ray light curve are similar to those obtained from optical data. Given the signal-to-noise of the late X-ray data and possible contamination from flares, it is difficult to distinguish the two models from the X-ray data alone. Instead, since the properties of the optical afterglow are better constrained, we raise the question whether the X-ray afterglow is consistent with the best fit optical model. The fitting results show that they are consistent, i.e., the optical and X-ray data are consistent with an achromatic broken power-law model with superimposed flares.

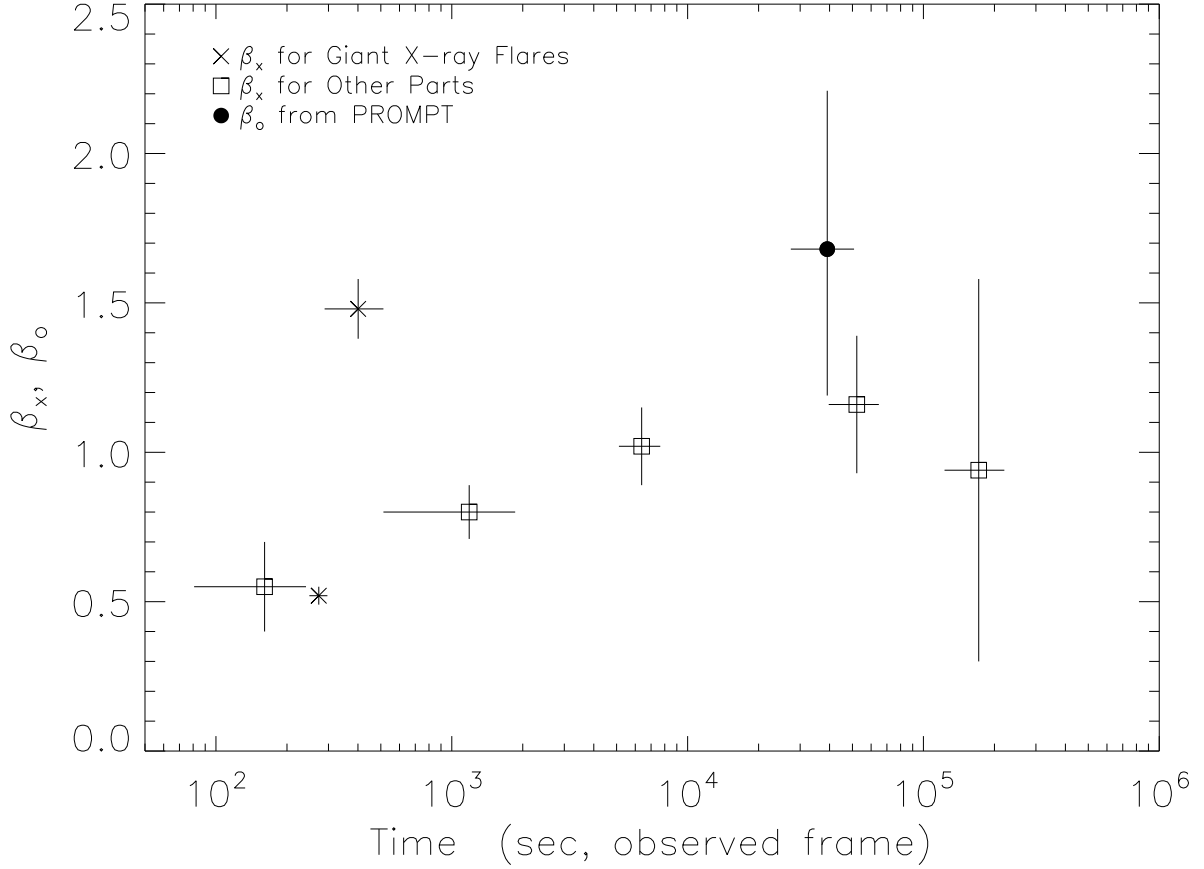


Fig. 3.— The evolution of X-ray and optical afterglow spectral indices ( $\beta_X$  and  $\beta_o$ ) of GRB 060526. The “X” symbols are the X-ray spectral indices for the two giant X-ray flares, and the squares are for other parts of the X-ray afterglow. The filled circle is the optical spectral index obtained from PROMPT’s  $B, r', i'$  bands.



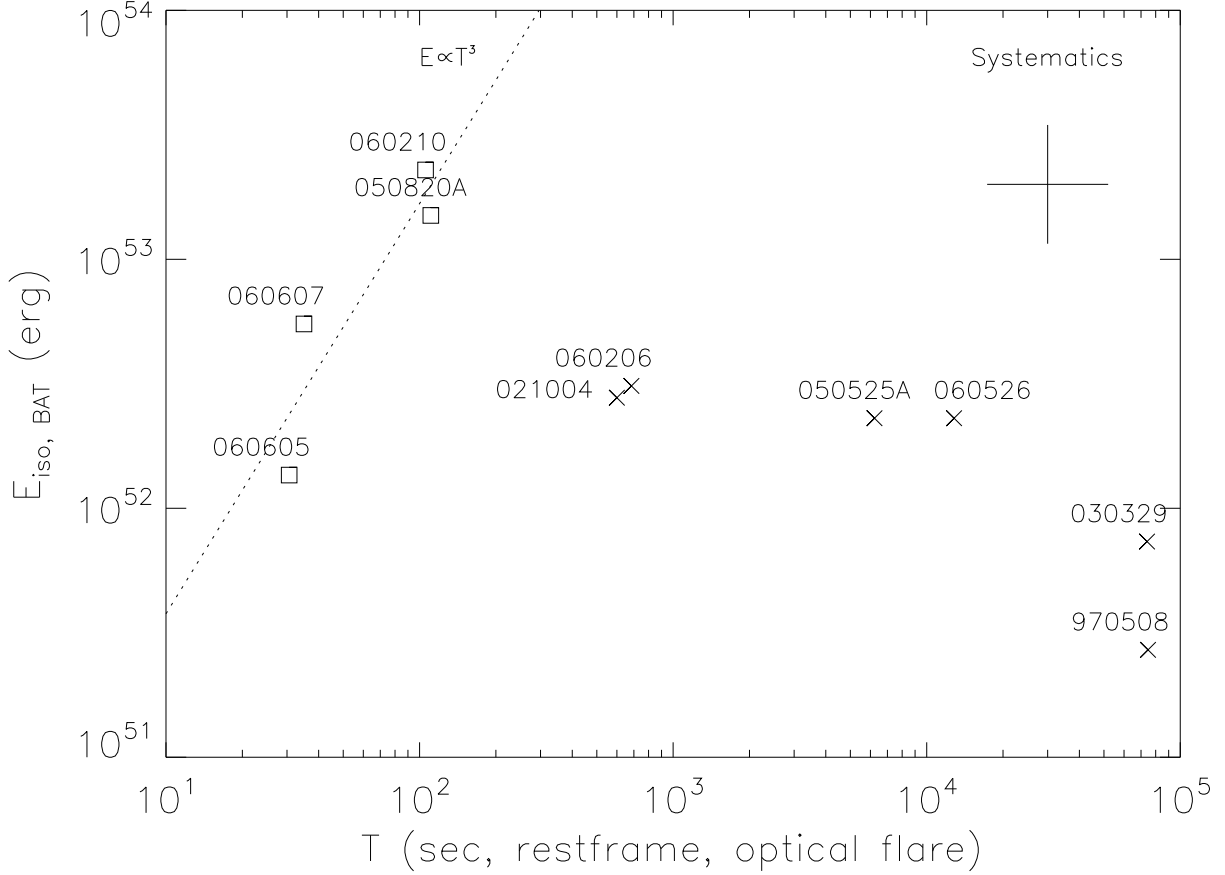


Fig. 4.— Isotropic energy in the BAT band versus optical flare time for GRBs with significant optical flares. We expect a factor of a few (3 in the plot as an example) for systematic uncertainties affecting the data points. Overall, no positive correlation between isotropic energy and flare time is found from this data set. However, a subset of the sample follows the prediction on the onset of the afterglow  $T \propto E_{iso}^{1/3}$  (dotted line). We notice the difference between the flares that occur before the afterglow has decayed (squares) and those afterward (“X” symbols). An important caveat is that the optical flare time is contingent on the initial optical observation of each event.

#### 4. Discussion

We present well-sampled optical and X-ray afterglow light curves of GRB 060526. As discussed in the previous section, the evolution of the afterglow is complicated with multiple breaks and flares both in the optical and the X-ray bands. The combination of flares and incomplete data sampling present severe challenges to measuring the temporal decay slopes of the afterglow, even for a well-sampled burst such as GRB 060526. Below, we proceed by assuming that our analysis results are not significantly affected by these factors.

We detected a possible achromatic jet break in the optical and X-ray afterglow light curves. Before this late-time break ( $T \sim 2.4 \times 10^5$  sec), the afterglow is consistent with many *Swift* afterglows (Nousek et al. 2006). The X-ray light curve started with a steep decay ( $\alpha_1 = 2.3 \pm 0.2$ ), which is interpreted as the tail of the prompt emission due to the “curvature effect” (Kumar & Panaitescu 2000). The spectral and temporal indices are constrained as  $\alpha = \beta + 2$ , which is consistent with the X-ray spectral index of  $\beta_1 = 0.55 \pm 0.15$ . The X-ray light curve then entered into a shallow decay stage with  $\alpha_2 \sim 0.5$ , which we interpret as energy injection. Then it decays into a normal afterglow stage with  $\alpha_3 = 1.14 \pm 0.02$  as constrained from the optical observations. In addition, the X-ray light curve shows two huge flares which are commonly seen in *Swift* X-ray afterglows and are attributed to late time central engine activities. After the achromatic break, the afterglow enters a very steep stage with  $\alpha_4 = 3.4 \pm 0.2$ . The X-ray and optical-to-X-ray spectral indices after 5000 sec are consistent with  $\sim 1$ , suggesting that the optical and X-ray bands are on the same power-law segment of the spectral energy distribution. The optical spectral index is marginally consistent with the X-ray index, although the error-bar is large.

The achromatic break observed in optical afterglows is traditionally interpreted as the jet break. As mentioned in the introduction, the achromatic break is not yet confirmed across optical and X-ray light curves. Here, we present a case in GRB 060526 where such an achromatic break is observed across the optical and X-ray afterglows, supporting the beaming model of the GRBs. However, the afterglow decay slopes before and after the break are hard to reconcile with simple afterglow-jet models. The late time decay slope after the jet break should follow  $\alpha = p$  (Sari et al. 1999), where  $p$  is power-law index for the electrons  $N(\gamma) \propto \gamma^{-p}$ . The post-jet slope,  $3.4 \pm 0.2$ , is too steep for a pre-jet slope of  $1.14 \pm 0.02$  under any combination of either constant or wind medium and relative positions between  $\nu$ ,  $\nu_m$ , and  $\nu_c$ . Since the achromatic break is most easily explained by a jet, it is possible that more complicated afterglow models are needed (e.g., Panaitescu et al. 2006) with non-standard micro-physical parameters. Another possibility is that energy injection or flares continued contributing significant flux and significantly affected the temporal decay slope. We estimated the jet angle (half opening angle for uniform jets or observer’s viewing angle

for structured jets) using  $t_j \simeq 6.2(E_{52}/n)^{1/3}(\theta_j/0.1)^{8/3}$  hr (Sari et al. 1999) and obtained  $\theta_j \sim 7^\circ$  assuming ambient density  $n = 1 \text{ cm}^{-3}$ . We further estimated the size of the  $\gamma$ -ray prompt emission by combining the measured jet angle and the X-ray tail emission detected before 225 sec using  $t_{tail} = (1+z)(R_{prompt}/c)(\theta_j^2/2)$  (Zhang et al. 2006) and obtained  $R_{prompt} \sim 2 \times 10^{14}$  cm.

We also observed multiple optical flares in the light curve of GRB 060526. Optical flares or re-brightenings have been observed in both pre-*Swift* (e.g., GRB 970508, GRB 021004, and GRB 030329, Galama et al. 1998; Lazzati et al. 2002; Bersier et al. 2003; Mirabal et al. 2003; Lipkin et al. 2004) and *Swift* bursts (e.g., GRB 050525A, GRB 050820A, GRB 060206, GRB 060210, GRB 060605, and GRB 060607, Blustin et al. 2006; Cenko et al. 2006; Stanek et al. 2006; Schaefer et al. 2006; Nysewander et al. 2006). The fraction of bursts with optical flares seemed small. However, recently many well-sampled bursts show complex optical decay behaviors. The accumulating observations argue that it is possible that most of optical afterglows are complex and the appearance of simplicity was a consequence of poor sampling. There are several interpretations for the optical flares, such as models of density fluctuations, “patchy shell”, “refreshed shock”, and late central engine activities (e.g., Ioka et al. 2005). We estimated the quantities  $\Delta t/t \sim 0.16, 0.6,$  and  $0.2$  and  $\Delta F_\nu/F_\nu \sim 0.2, 0.7,$  and  $0.2$ , respectively, for the three flares detected in GRB 060526. The  $\Delta t/t$  values are small arguing against the models of patchy shell and refreshed shock, since the model predictions are  $\Delta t/t > 1$  and  $> 1/4$  for these two models (Ioka et al. 2005). The properties of the flares barely satisfy Ioka et al.’s constraint,  $\Delta F_\nu/F_\nu < 1.6\Delta t/t$ , under the density fluctuation model. Recently, Nakar & Granot (2006) also modeled the effects of density fluctuations on the afterglow light curves and found that they cannot produce the sharp features observed in many bursts. Another possibility is that the flares (or breaks) indicate the onset of the afterglow (Rykoff et al. 2006; Stanek et al. 2006) scaled with the isotropic energy as  $T_{onset} \propto E_{iso}^{1/3}$  (Sari 1997). The onset time also depends on the density of the ambient medium and the initial Lorentz factor that are more difficult to measure. We might expect a correlation between  $E_{iso}$  and  $T_{onset}$  for a large sample of bursts, or if the densities and Lorentz factors for the bursts only spread in a narrow range. We tested this hypothesis by plotting the two properties for bursts with optical flares in Fig. 4, and did not detect positive correlation between the two properties. However, we notice the difference between flares that occur before the optical afterglow has decayed and those that occur afterward. The flares in GRB 050820A, GRB 060210, GRB 060605, and GRB 060607 possibly belong to the category of flares that occur before the afterglow has faded, and they roughly follow the scaling between isotropic energy and flare time. However, a larger sample is needed to fully test the model. In any case, the flares in GRB 060526 are unlikely to be associated with the onset of the afterglow. Therefore, we are left with the possibility that the flares in

GRB 060526 are from late central engine activities.

We acknowledge the *Swift* team for the prompt detection and localization of the GRB and the rapid release of data products. We also thank the GRB Coordinates Network (GCN) and astronomers who contribute to the GCN circular. We thank B. Zhang for helpful discussion.

## REFERENCES

- Arnaud, K.A., 1996, ASP Conf. Ser. 101: Astronomical Data Analysis Software and Systems V, ed. Jacoby G. & Barnes J., 17
- Baliyan, K. S., et al. 2006, GCN 5185
- Berger, E. & Gladders, M. 2006, GCN 5170
- Bersier, D., et al. 2003, ApJ, 584, L43
- Blustin, A. J., et al. 2006, ApJ, 637, 901
- Campana, S., et al. 2006, GCN 5162
- Campana, S., et al. 2006, GCN 5168
- Cenko, S. B., et al. 2006, astro-ph/0608183
- Covino, S. et al. 2006, GCN 5167
- Dai, X., & Zhang, B. 2005, ApJ, 621, 875
- Frail, D. A., et al. 2001, ApJ, 562, L55
- French, J. & Jelinek, M. 2006, GCN 5165
- Galama, T. J., et al. 1998, ApJ, 497, L13
- Gehrels, N., et al. 2004, ApJ, 611, 1005
- Ioka, K., Kobayashi, S., & Zhang, B. 2005, ApJ, 631, 429
- Kann, D. A., & Hoegner, C. 2006, GCN 5182
- Khamitov, I., et al. 2006a, GCN 5173

- Khamitov, I., et al. 2006b, GCN 5177
- Khamitov, I., et al. 2006c, GCN 5183
- Khamitov, I., et al. 2006d, GCN 5186
- Khamitov, I., et al. 2006e, GCN 5189
- Khamitov, I., et al. 2006f, GCN 5193
- Kumar, P., & Panaitescu, A. 2000, ApJ, 541, L51
- Lamb, D. Q., Donaghy, T. Q., & Graziani, C. 2005, ApJ, 620, 355
- Lazzati, D., Rossi, E., Covino, S., Ghisellini, G., & Malesani, D. 2002, A&A, 396, L5
- Lin, C. S., et al. 2006, GCN 5169
- Lipkin, Y. M., et al. 2004, ApJ, 606, L381
- Lloyd-Ronning, N. M., Dai, X., & Zhang, B. 2004, ApJ, 601, 371
- Mészáros, P., & Rees, M. J. 1997, ApJ, 476, 232
- Mirabal, N., et al. 2003, ApJ, 595, 935
- Monfardini, A., et al. 2006, astro-ph/0603181
- Nakar, E., & Granot, J. 2006, astro-ph/0606011
- Nousek, J. A., et al. 2006, ApJ, 642, 389
- Nysewander, M., et al. 2006, GCN 5236
- O’Brien, P. T., et al. 2006, astro-ph/0601125
- Panaitescu, A., Mészáros, P., Burrows, D., Nousek, J., Gehrels, N., O’Brien, P., & Willingale, R. 2006, MNRAS, 595
- Rhoads, J. E. 1999, ApJ, 525, 737
- Rossi, E., Lazzati, D., & Rees, M. J. 2002, MNRAS, 332, 945
- Rumyantsev, V., et al. 2006a, GCN 5181
- Rumyantsev, V., et al. 2006b, GCN 5306

- Rykoff, E. S., et al. 2006, ApJ, 638, L5
- Sari, R. 1997, ApJ, 489, L37
- Sari, R., Piran, T., & Halpern, J. P. 1999, ApJ, 519, L17
- Sari, R., Piran, T., & Narayan, R. 1998, ApJ, 497, L17
- Schaefer, B. E., et al. 2006, GCN 5222
- Stanek, K. Z., Dai, X., Prieto, J. L., et al. 2006, submitted to ApJ Letter, astro-ph/0602495
- Stanek, K. Z., Garnavich, P. M., Kaluzny, J., Pych, W., & Thompson, I. 1999, ApJ, 522, L39
- Terra, F., et al. 2006, GCN 5192
- Yamazaki, R., Ioka, K., & Nakamura, T. 2003, ApJ, 593, 941
- Zhang, B., Dai, X., Lloyd-Ronning, N. M., & Mészáros, P. 2004, ApJ, 601, L119
- Zhang, B. & Mészáros, P. 2002, ApJ, 571, 876
- Zhang, B., Fan, Y. Z., Dyks, J., Kobayashi, S., Mészáros, P., Burrows, D. N., Nousek, J. A., & Gehrels, N. 2006, ApJ, 642, 354

Table 1. Optical and X-ray Light Curves of GRB 060526.

Telescope	Time (sec)	Band	Mode	Magnitude	Count Rate (count s <sup>-1</sup> )
MDM 1.3m	39744	R	...	19.75±0.04	...
MDM 1.3m	40349	R	...	19.83±0.04	...
MDM 1.3m	41040	R	...	19.77±0.03	...
MDM 1.3m	41645	R	...	19.80±0.03	...
MDM 1.3m	42250	R	...	19.89±0.03	...
MDM 1.3m	42941	R	...	19.80±0.03	...
MDM 1.3m	43546	R	...	19.89±0.03	...
MDM 1.3m	44150	R	...	19.87±0.03	...
MDM 1.3m	44842	R	...	19.95±0.04	...
MDM 1.3m	45619	R	...	19.95±0.03	...
MDM 1.3m	46483	R	...	19.97±0.03	...
MDM 1.3m	47088	R	...	19.90±0.03	...
MDM 1.3m	47779	R	...	19.97±0.03	...
MDM 1.3m	48384	R	...	20.09±0.04	...
MDM 1.3m	49075	R	...	20.01±0.03	...
MDM 1.3m	49680	R	...	20.12±0.04	...
MDM 1.3m	50458	R	...	20.10±0.04	...
MDM 1.3m	51322	R	...	20.20±0.04	...
MDM 1.3m	51926	R	...	20.08±0.04	...
MDM 1.3m	52531	R	...	20.11±0.04	...
MDM 1.3m	53222	R	...	20.08±0.04	...
MDM 1.3m	53827	R	...	20.07±0.04	...
MDM 1.3m	54432	R	...	20.20±0.04	...
MDM 1.3m	55123	R	...	20.16±0.04	...
MDM 1.3m	55728	R	...	20.14±0.04	...
MDM 1.3m	56333	R	...	20.18±0.04	...
MDM 1.3m	57024	R	...	20.13±0.04	...
MDM 1.3m	57629	R	...	20.19±0.04	...
MDM 1.3m	58234	R	...	20.17±0.04	...
MDM 1.3m	58925	R	...	20.10±0.04	...
MDM 1.3m	59530	R	...	20.03±0.04	...
MDM 1.3m	60221	R	...	20.03±0.04	...
MDM 1.3m	60826	R	...	20.15±0.04	...
MDM 1.3m	61430	R	...	20.07±0.04	...
MDM 1.3m	62122	R	...	20.14±0.04	...
MDM 1.3m	62726	R	...	20.06±0.04	...
MDM 1.3m	63331	R	...	20.20±0.05	...
MDM 1.3m	64022	R	...	20.24±0.06	...
MDM 1.3m	64627	R	...	20.22±0.05	...
MDM 1.3m	65232	R	...	20.22±0.06	...
MDM 1.3m	126230	R	...	20.91±0.11	...
MDM 1.3m	126835	R	...	20.74±0.07	...
MDM 1.3m	127526	R	...	20.79±0.07	...
MDM 1.3m	128131	R	...	20.97±0.09	...
MDM 1.3m	129082	R	...	20.80±0.07	...

Table 1—Continued

Telescope	Time (sec)	Band	Mode	Magnitude	Count Rate (count s <sup>-1</sup> )
MDM 1.3m	129773	R	...	20.86±0.08	...
MDM 1.3m	130550	R	...	20.69±0.08	...
MDM 1.3m	131155	R	...	20.92±0.09	...
MDM 1.3m	131760	R	...	20.85±0.08	...
MDM 1.3m	132451	R	...	21.04±0.10	...
MDM 1.3m	133142	R	...	20.94±0.08	...
MDM 1.3m	133747	R	...	21.01±0.09	...
MDM 1.3m	134438	R	...	20.87±0.07	...
MDM 1.3m	135043	R	...	20.99±0.07	...
MDM 1.3m	135648	R	...	21.06±0.08	...
MDM 1.3m	136339	R	...	21.03±0.09	...
MDM 1.3m	136944	R	...	21.23±0.10	...
MDM 1.3m	137549	R	...	21.31±0.11	...
MDM 1.3m	138326	R	...	21.22±0.09	...
MDM 1.3m	138931	R	...	21.14±0.08	...
MDM 1.3m	139536	R	...	21.15±0.08	...
MDM 1.3m	140227	R	...	21.05±0.08	...
MDM 1.3m	140832	R	...	21.20±0.09	...
MDM 1.3m	141437	R	...	21.10±0.07	...
MDM 1.3m	142128	R	...	21.11±0.08	...
MDM 1.3m	142733	R	...	21.30±0.10	...
MDM 1.3m	143338	R	...	21.25±0.11	...
MDM 1.3m	144029	R	...	21.09±0.09	...
MDM 1.3m	144634	R	...	21.25±0.10	...
MDM 1.3m	145238	R	...	21.24±0.10	...
MDM 1.3m	145930	R	...	21.23±0.10	...
MDM 1.3m	146534	R	...	21.33±0.11	...
MDM 1.3m	147139	R	...	21.28±0.10	...
MDM 1.3m	147830	R	...	21.17±0.09	...
MDM 1.3m	148435	R	...	21.27±0.10	...
MDM 1.3m	149040	R	...	21.24±0.10	...
MDM 1.3m	149731	R	...	21.11±0.09	...
MDM 1.3m	150336	R	...	21.23±0.11	...
MDM 1.3m	150941	R	...	21.29±0.11	...
MDM 1.3m	213667	R	...	22.04±0.06	...
MDM 1.3m	216605	R	...	22.02±0.05	...
MDM 1.3m	234576	R	...	22.19±0.04	...
MDM 1.3m	302054	R	...	22.62±0.07	...
MDM 2.4m	39658	R	...	19.78±0.03	...
MDM 2.4m	40176	R	...	19.76±0.02	...
MDM 2.4m	49248	R	...	20.03±0.02	...
MDM 2.4m	62813	R	...	20.10±0.03	...
MDM 2.4m	126576	R	...	20.83±0.03	...
MDM 2.4m	134784	R	...	20.97±0.02	...
MDM 2.4m	149040	R	...	21.15±0.03	...



Table 1—Continued

Telescope	Time (sec)	Band	Mode	Magnitude	Count Rate (count s <sup>-1</sup> )
MDM 2.4m	150336	R	...	21.17±0.02	...
MDM 2.4m	156211	R	...	21.20±0.03	...
MDM 2.4m	221443	R	...	21.90±0.06	...
MDM 2.4m	222826	R	...	21.97±0.03	...
MDM 2.4m	307411	R	...	22.63±0.03	...
MDM 2.4m	312422	R	...	22.52±0.02	...
MDM 2.4m	396144	R	...	23.50±0.04	...
MDM 2.4m	397440	R	...	23.56±0.04	...
PROMPT	27000	B	...	20.73±0.08	...
PROMPT	36000	B	...	21.36±0.09	...
PROMPT	43560	B	...	21.33±0.09	...
PROMPT	48960	B	...	21.85±0.15	...
PROMPT	55440	B	...	21.94±0.22	...
PROMPT	27360	r'	...	19.49±0.04	...
PROMPT	29880	r'	...	19.77±0.05	...
PROMPT	37440	r'	...	20.01±0.05	...
PROMPT	39960	r'	...	20.09±0.08	...
PROMPT	47880	r'	...	20.22±0.07	...
PROMPT	50760	r'	...	20.43±0.08	...
PROMPT	24840	i'	...	19.22±0.06	...
PROMPT	32760	i'	...	19.56±0.06	...
PROMPT	35280	i'	...	19.77±0.06	...
PROMPT	42480	i'	...	19.79±0.06	...
PROMPT	45000	i'	...	19.97±0.04	...
PROMPT	53640	i'	...	20.00±0.08	...
PROMPT	57240	i'	...	19.98±0.10	...
<i>Swift</i>	84	0.2–10 keV	WT	...	7.60±1.23
<i>Swift</i>	89	0.2–10 keV	WT	...	8.40±1.33
<i>Swift</i>	94	0.2–10 keV	WT	...	4.80±1.02
<i>Swift</i>	99	0.2–10 keV	WT	...	5.20±1.06
<i>Swift</i>	104	0.2–10 keV	WT	...	3.00±0.87
<i>Swift</i>	109	0.2–10 keV	WT	...	4.20±1.04
<i>Swift</i>	114	0.2–10 keV	WT	...	4.80±1.06
<i>Swift</i>	119	0.2–10 keV	WT	...	4.40±0.94
<i>Swift</i>	124	0.2–10 keV	WT	...	3.40±0.87
<i>Swift</i>	129	0.2–10 keV	WT	...	4.00±0.89
<i>Swift</i>	239	0.2–10 keV	WT	...	72.40±3.83
<i>Swift</i>	244	0.2–10 keV	WT	...	142.20±5.36
<i>Swift</i>	249	0.2–10 keV	WT	...	321.80±8.06
<i>Swift</i>	254	0.2–10 keV	WT	...	312.00±7.96
<i>Swift</i>	259	0.2–10 keV	WT	...	276.80±7.50
<i>Swift</i>	264	0.2–10 keV	WT	...	233.60±6.90
<i>Swift</i>	269	0.2–10 keV	WT	...	206.60±6.43
<i>Swift</i>	274	0.2–10 keV	WT	...	164.40±5.80
<i>Swift</i>	279	0.2–10 keV	WT	...	133.60±5.20

Table 1—Continued

Telescope	Time (sec)	Band	Mode	Magnitude	Count Rate (count s <sup>-1</sup> )
<i>Swift</i>	284	0.2–10 keV	WT	...	115.60±4.83
<i>Swift</i>	289	0.2–10 keV	WT	...	105.00±4.59
<i>Swift</i>	294	0.2–10 keV	WT	...	151.20±5.54
<i>Swift</i>	299	0.2–10 keV	WT	...	178.60±6.01
<i>Swift</i>	304	0.2–10 keV	WT	...	172.00±5.89
<i>Swift</i>	309	0.2–10 keV	WT	...	167.00±5.79
<i>Swift</i>	314	0.2–10 keV	WT	...	155.80±5.63
<i>Swift</i>	319	0.2–10 keV	WT	...	149.80±5.49
<i>Swift</i>	324	0.2–10 keV	WT	...	150.80±5.51
<i>Swift</i>	329	0.2–10 keV	WT	...	136.80±5.24
<i>Swift</i>	334	0.2–10 keV	WT	...	128.00±5.11
<i>Swift</i>	339	0.2–10 keV	WT	...	116.80±4.87
<i>Swift</i>	344	0.2–10 keV	WT	...	94.60±4.35
<i>Swift</i>	349	0.2–10 keV	WT	...	81.40±4.03
<i>Swift</i>	354	0.2–10 keV	WT	...	66.00±3.67
<i>Swift</i>	359	0.2–10 keV	WT	...	52.80±3.27
<i>Swift</i>	364	0.2–10 keV	WT	...	47.60±3.11
<i>Swift</i>	369	0.2–10 keV	WT	...	36.40±2.73
<i>Swift</i>	374	0.2–10 keV	WT	...	40.80±2.88
<i>Swift</i>	379	0.2–10 keV	WT	...	33.00±2.62
<i>Swift</i>	384	0.2–10 keV	WT	...	27.00±2.34
<i>Swift</i>	389	0.2–10 keV	WT	...	25.20±2.28
<i>Swift</i>	394	0.2–10 keV	WT	...	19.60±2.00
<i>Swift</i>	399	0.2–10 keV	WT	...	15.00±1.78
<i>Swift</i>	404	0.2–10 keV	WT	...	17.40±1.89
<i>Swift</i>	409	0.2–10 keV	WT	...	14.60±1.71
<i>Swift</i>	414	0.2–10 keV	WT	...	13.60±1.67
<i>Swift</i>	419	0.2–10 keV	WT	...	11.20±1.57
<i>Swift</i>	424	0.2–10 keV	WT	...	11.20±1.50
<i>Swift</i>	429	0.2–10 keV	WT	...	7.60±1.23
<i>Swift</i>	434	0.2–10 keV	WT	...	8.80±1.33
<i>Swift</i>	439	0.2–10 keV	WT	...	7.40±1.28
<i>Swift</i>	444	0.2–10 keV	WT	...	7.80±1.25
<i>Swift</i>	449	0.2–10 keV	WT	...	7.60±1.30
<i>Swift</i>	454	0.2–10 keV	WT	...	7.20±1.20
<i>Swift</i>	459	0.2–10 keV	WT	...	6.20±1.18
<i>Swift</i>	464	0.2–10 keV	WT	...	4.80±1.02
<i>Swift</i>	469	0.2–10 keV	WT	...	5.00±1.00
<i>Swift</i>	474	0.2–10 keV	WT	...	7.00±1.22
<i>Swift</i>	479	0.2–10 keV	WT	...	4.20±0.96
<i>Swift</i>	484	0.2–10 keV	WT	...	3.80±0.87
<i>Swift</i>	489	0.2–10 keV	WT	...	3.60±0.94
<i>Swift</i>	494	0.2–10 keV	WT	...	4.00±0.94
<i>Swift</i>	499	0.2–10 keV	WT	...	2.80±0.75
<i>Swift</i>	504	0.2–10 keV	WT	...	2.20±0.77

Table 1—Continued

Telescope	Time (sec)	Band	Mode	Magnitude	Count Rate (count s <sup>-1</sup> )
<i>Swift</i>	509	0.2–10 keV	WT	...	3.80±0.87
<i>Swift</i>	514	0.2–10 keV	WT	...	2.00±0.63
<i>Swift</i>	138	0.2–10 keV	PC	...	1.7436±0.6026
<i>Swift</i>	143	0.2–10 keV	PC	...	1.8000±0.6000
<i>Swift</i>	148	0.2–10 keV	PC	...	1.8000±0.6000
<i>Swift</i>	153	0.2–10 keV	PC	...	1.4000±0.5292
<i>Swift</i>	158	0.2–10 keV	PC	...	2.0000±0.6325
<i>Swift</i>	163	0.2–10 keV	PC	...	2.2872±0.6974
<i>Swift</i>	168	0.2–10 keV	PC	...	2.4000±0.6928
<i>Swift</i>	173	0.2–10 keV	PC	...	1.7436±0.6026
<i>Swift</i>	178	0.2–10 keV	PC	...	2.0000±0.6325
<i>Swift</i>	183	0.2–10 keV	PC	...	2.6000±0.7211
<i>Swift</i>	188	0.2–10 keV	PC	...	1.5436±0.5685
<i>Swift</i>	193	0.2–10 keV	PC	...	0.7436±0.4040
<i>Swift</i>	198	0.2–10 keV	PC	...	0.8000±0.4000
<i>Swift</i>	203	0.2–10 keV	PC	...	1.0000±0.4472
<i>Swift</i>	208	0.2–10 keV	PC	...	0.4000±0.2828
<i>Swift</i>	213	0.2–10 keV	PC	...	1.2000±0.4899
<i>Swift</i>	218	0.2–10 keV	PC	...	1.3436±0.5321
<i>Swift</i>	223	0.2–10 keV	PC	...	0.7436±0.4040
<i>Swift</i>	228	0.2–10 keV	PC	...	2.7436±0.7505
<i>Swift</i>	586	0.2–10 keV	PC	...	1.2844±0.1136
<i>Swift</i>	686	0.2–10 keV	PC	...	0.7915±0.0896
<i>Swift</i>	786	0.2–10 keV	PC	...	0.5000±0.0707
<i>Swift</i>	886	0.2–10 keV	PC	...	0.3203±0.0588
<i>Swift</i>	986	0.2–10 keV	PC	...	0.3015±0.0559
<i>Swift</i>	1086	0.2–10 keV	PC	...	0.2972±0.0548
<i>Swift</i>	1186	0.2–10 keV	PC	...	0.2944±0.0549
<i>Swift</i>	1286	0.2–10 keV	PC	...	0.2415±0.0502
<i>Swift</i>	1386	0.2–10 keV	PC	...	0.1687±0.0428
<i>Swift</i>	1486	0.2–10 keV	PC	...	0.1744±0.0426
<i>Swift</i>	1586	0.2–10 keV	PC	...	0.2515±0.0512
<i>Swift</i>	1686	0.2–10 keV	PC	...	0.2559±0.0523
<i>Swift</i>	1786	0.2–10 keV	PC	...	0.1500±0.0387
<i>Swift</i>	5186	0.2–10 keV	PC	...	0.1415±0.0390
<i>Swift</i>	5286	0.2–10 keV	PC	...	0.0800±0.0283
<i>Swift</i>	5386	0.2–10 keV	PC	...	0.0844±0.0303
<i>Swift</i>	5486	0.2–10 keV	PC	...	0.1315±0.0377
<i>Swift</i>	5586	0.2–10 keV	PC	...	0.1431±0.0406
<i>Swift</i>	5686	0.2–10 keV	PC	...	0.1287±0.0378
<i>Swift</i>	5786	0.2–10 keV	PC	...	0.1603±0.0431
<i>Swift</i>	5886	0.2–10 keV	PC	...	0.0787±0.0305
<i>Swift</i>	5986	0.2–10 keV	PC	...	0.0887±0.0321
<i>Swift</i>	6086	0.2–10 keV	PC	...	0.1074±0.0369
<i>Swift</i>	6186	0.2–10 keV	PC	...	0.0944±0.0319

Table 1—Continued

Telescope	Time (sec)	Band	Mode	Magnitude	Count Rate (count s <sup>-1</sup> )
<i>Swift</i>	6286	0.2–10 keV	PC	...	0.1503±0.0419
<i>Swift</i>	6386	0.2–10 keV	PC	...	0.1115±0.0350
<i>Swift</i>	6486	0.2–10 keV	PC	...	0.1844±0.0438
<i>Swift</i>	6586	0.2–10 keV	PC	...	0.1615±0.0415
<i>Swift</i>	6686	0.2–10 keV	PC	...	0.1815±0.0439
<i>Swift</i>	6786	0.2–10 keV	PC	...	0.0846±0.0342
<i>Swift</i>	6886	0.2–10 keV	PC	...	0.0931±0.0339
<i>Swift</i>	6986	0.2–10 keV	PC	...	0.0646±0.0312
<i>Swift</i>	7086	0.2–10 keV	PC	...	0.1046±0.0370
<i>Swift</i>	7186	0.2–10 keV	PC	...	0.1159±0.0366
<i>Swift</i>	7286	0.2–10 keV	PC	...	0.0759±0.0307
<i>Swift</i>	7386	0.2–10 keV	PC	...	0.0872±0.0301
<i>Swift</i>	7486	0.2–10 keV	PC	...	0.0787±0.0305
<i>Swift</i>	7586	0.2–10 keV	PC	...	0.2072±0.0459
<i>Swift</i>	40173	0.2–10 keV	PC	...	0.0121±0.0065
<i>Swift</i>	46173	0.2–10 keV	PC	...	0.0257±0.0078
<i>Swift</i>	51673	0.2–10 keV	PC	...	0.0202±0.0074
<i>Swift</i>	52173	0.2–10 keV	PC	...	0.0041±0.0052
<i>Swift</i>	52673	0.2–10 keV	PC	...	0.0101±0.0062
<i>Swift</i>	63673	0.2–10 keV	PC	...	0.0135±0.0057
<i>Swift</i>	64173	0.2–10 keV	PC	...	0.0172±0.0071
<i>Swift</i>	139785	0.2–10 keV	PC	...	0.0026±0.0009
<i>Swift</i>	168735	0.2–10 keV	PC	...	0.0017±0.0008
<i>Swift</i>	200435	0.2–10 keV	PC	...	0.0022±0.0009
<i>Swift</i>	243601	0.2–10 keV	PC	...	0.0019±0.0007
<i>Swift</i>	284976	0.2–10 keV	PC	...	0.0007±0.0006
<i>Swift</i>	341833	0.2–10 keV	PC	...	0.0003±0.0004
<i>Swift</i>	504585	0.2–10 keV	PC	...	0.0003±0.0003
<i>Swift</i>	417948	0.2–10 keV	PC	...	0.0004±0.0003